Seismic Signature of Rain and Wind Inferred From Seismic Data

E. Rindraharisaona, A. Réchou, F. Fontaine, G. Barruol, P. Stamenoff, B. Boudevillain, F. Rigaud-Louise, E. Delcher

AGU ADVANCING EARTH AND SPACE SCIENCE

Earth and Space Science

RESEARCH ARTICLE
10.1029/2022EA002328

Key Points:

- At frequencies >1 Hz different seismic responses overlap in frequency range and the observed spectra represent their cumulative effects
- The rain precipitation and wind intensity are strongly correlated with the seismic noise at frequencies >80 Hz
- Different seismic responses are observed according to the soil types the instrument is emplaced in

Supporting Information:

Supporting Information may be found in the online version of this article.

Correspondence to:

E. J. Rindraharisaona,
elisa.rindraharisaona@univ-reunion.fr

Citation:

Rindraharisaona, E. J., Réchou, A., Fontaine, F. R., Barruol, G., Stamenoff, P., Boudevillain, B., et al. (2022). Seismic signature of rain and wind inferred from seismic data. *Earth and Space Science*, *9*, e2022EA002328. https://doi.org/10.1029/2022EA002328

Received 16 MAR 2022
Accepted 6 OCT 2022

Author Contributions:

Data curation: E. J. Rindraharisaona, A. Réchou, P. Stamenoff, F. Rigaud-Louise, E. Delcher
Formal analysis: E. J. Rindraharisaona
Funding acquisition: E. J. Rindraharisaona, A. Réchou, F. R. Fontaine
Methodology: E. J. Rindraharisaona, F. R. Fontaine, G. Barruol, B. Boudevillain

Seismic Signature of Rain and Wind Inferred From Seismic Data

E. J. Rindraharisaona[1,2], A. Réchou[3], F. R. Fontaine[1,4], G. Barruol[5], P. Stamenoff[6], B. Boudevillain[5], F. Rigaud-Louise[3], and E. Delcher[1,2]

[1]Institut de physique du globe de Paris, CNRS, Université de Paris, Paris, France, [2]Laboratoire GéoSciences Réunion, Université de La Réunion, Saint Denis, France, [3]Météo France, CNRS, Laboratoire du LACy, Réunion, Université de la Réunion, Saint Denis, France, [4]Observatoire volcanologique et sismologique de la Martinique, Institut de physique du globe de Paris, Fonds Saint Denis, France, [5]CNRS, IRD, Grenoble INP, IGE, Université Grenoble Alpes, Grenoble, France, [6]Observatoire des Sciences de l'Univers de la Réunion, UAR 3365, Université de la Réunion, Saint Denis, France

Abstract Seismic stations are increasingly used to monitor river activity and to quantify sediment transport during flood events. In tropical regions, cyclone-induced floods are often associated with heavy rain and strong wind episodes, generating complex seismic records involving the simultaneous signature of water, sediment, rainfall and wind. Hence, seismic characterization of rain and wind is then required to better decipher each process and improve our understanding of the river seismic signature. In this study, we investigate experimentally the seismic response of rain and wind using data recorded by geophones deployed in various soil types and at different burial depth (BD), co-located with various meteorological instruments. Our results show that the power spectral density (PSD) of the seismic noise intensifies at a frequency between 60 and 500 Hz for rain and 5 and 500 Hz for wind, in the presence of rain precipitation as low as 0.025 mm/min and/or wind speed ≥3 m/s. PSD analysis indicates that the seismic signal associated with rain decreases with the BD with a value of ∼2–5 dB in a depth difference of 10 cm. We also observe that each soil type has its own seismic signature. The 4-min root mean square correlation between the seismic signal amplitude and the rain precipitation suggests that they best correlate with Pearson coefficient >0.90 at BD of 30 cm. The transfer function between the precipitation rate (or kinetic energy) and the seismic signal amplitude shows that the signal recorded by the geophone can be used as a robust proxy for these parameters.

Plain Language Summary In addition to recording deep Earth activity such as earthquakes or volcanic eruptions, seismic sensors can measure numbers of naturally-induced ground vibrations such as those generated by rivers activities. In tropical areas during cyclonic events, heavy rain (and strong wind) leads to the presence of severe flooding, during which several activities in and on the river (e.g., sediment transport, wind, water, and rain) generate ground vibration, making the overall signals recorded by seismic sensors complex to interpret. To better decipher the river seismic signature, investigating the wind and rain signatures are then essential. In this study, we investigate experimentally the seismic response of rain and wind from data recorded by geophones and complemented by different meteorological sensors. The obtained results show that (a) the strength of the seismic noise intensifies with frequency for rain and wind; (b) the seismic signal associated with rain decreases with the burying depth of the sensor; (c) the amplitude of the seismic signal correlates with rain precipitation when the sensor is well buried and (d) the signal recorded by the geophone can be used as a robust proxy for rain precipitation.

1. Introduction

The natural risks associated with rain can result in significant environmental, infrastructure and human consequences. One of the major impacts of floods is the sediment transport along the rivers, that may destroy infrastructures alongside the rivers (e.g., Nwe & Tokuzo, 2010). Better monitoring of the river activity and the sediment transport could help to characterize the processes at play and to minimize the induced damages.

During the last few years, the cyclone impact on tropical islands has been the subject of a large multidisciplinary project called ReNovRisk involving atmosphere, hydrosphere, solid Earth and human sciences (Barthe et al., 2021; Bousquet et al., 2021; Tulet et al., 2021). In this frame, seismology has been used to analyze and quantify oceanic swells from terrestrial records (Rindraharisaona et al., 2020, 2021) and river activities during cyclonic floods (e.g., Gonzalez, 2019) to develop proxies for sediment transports, motivating finer signal analyses

Software: E. J. Rindraharisaona, B. Boudevillain
Validation: E. J. Rindraharisaona, A. Réchou, G. Barruol
Writing – original draft: E. J. Rindraharisaona
Writing – review & editing: E. J. Rindraharisaona, A. Réchou, F. R. Fontaine, G. Barruol, P. Stamenoff, B. Boudevillain, F. Rigaud-Louise, E. Delcher

such as the one proposed here. The ReNovRisk project focused mainly on the river activity in La Réunion Island in the SW Indian Ocean because this tropical region is particularly vulnerable to cyclonic episodes occurring during the Austral summer period (November–April). In addition, the presence of volcanic lithologies and the slope steepness characteristics of tropical volcanic islands such as La Réunion make it vulnerable to natural hazards such as landslides and rockfalls, closely related to rainfall, motivating also a better understanding of the rain activity to help decipher such destructive environmental processes.

From our knowledge, the specific question of the rain seismic signature is poorly documented in the literature. During the last decade(s), several experiments deployed seismic stations in the vicinity of rivers to monitor their activity (e.g., Burtin et al., 2008; Gonzalez, 2019; Roth et al., 2016), but only few of them focused on the rain signature itself (e.g., Bakker et al., 2022; Dean, 2017). Despite the different environments of these studies, they may all have recorded signals emitted by falling raindrops (Dean, 2017) and wind activity (e.g., Wilcock et al., 1999), which generally occur simultaneously in time and space, and potentially in overlapping frequency bands. Therefore, improvements in monitoring the river activity by seismic data requires a better understanding of the seismic signature of the rain and wind. Such an approach will be particularly helpful in studying landslides and/or rockfalls since the rain activity is a major triggering parameter of these hazardous processes (e.g., Guzzetti et al., 2007; Helmstetter & Garambois, 2010).

A key question in such experimental approach is the physical characteristic of the seismic sensor and its ability to record the rain signature. Seismic studies using a broadband seismometer (e.g., Roth et al., 2016) or a high frequency geophone (e.g., Dean, 2017) suggested that the seismic signature of the rain dominates at a frequency range of ∼80–480 Hz. Bakker et al. (2022) highlighted the importance of the contribution of the larger drops in the seismic signal. Their results also showed a power-law scaling relations between the seismic noise and the rain intensity (or kinetic energy). Detecting such rain signatures using a seismometer depends therefore on the sensor bandwidths, on its high cutting frequency and on the sampling frequency of the acquisition system. In the present work, we used geophones that can measure ground vibrations at frequencies as high as 500 Hz and a recording system at a sampling rate of 1,000 sample/s.

To better decipher the river noise from other signals, and particularly to better monitor the sediment transport during floods episodes, we developed in this current work an experimental approach to characterize and quantify the seismic signature of rain and wind recorded by seismic sensors (geophones) buried in different soil types and at different depths.

In the following, the spectral content recorded by the geophones at frequencies >1 Hz are analyzed to quantify and discuss the rain and wind signatures and particularly their frequency domains. Then the geophone responses for the different soil types and burial depths (BD) are evaluated. The amplitude of the recorded seismic noise is analyzed in light of meteorological parameters such as precipitation rate, wind intensity and rain kinetic energy. Finally, transfer functions are established between these variables.

2. Instrumental Setup, Data and Methods

The experiment took place in La Réunion, close to a sugarcane farm in the northern part of the island. Figure 1 describes the experimental site, where the seismic (geophones) and meteorological sensors (Campbell Scientific tipping bucket rain gauge ARG314, Vaisala WXT520 weather station and OTT Parsivel2 disdrometer) were deployed. To minimize the anthropogenic signals, we chose a site at some distance from frequent human activities, in our case, at ∼300 m from a highway and at ∼100 m from a side road with limited traffic (Figure 1).

We installed three vertical geophones, characterized by a natural frequency of 4.5 Hz with a spurious frequency ≥140 Hz, which is an important parameter fixing the maximum frequency useable for a geophone (Faber & Maxwell, 1997). In fact, the geophones used in this study have an instrument artifact at 140 Hz that generates interferences. To characterize the sensitivity of the seismic response with respect to the soil types, we made experiments with three different soil types such as sand, andisol (volcanic horizon soil) and gravel. We set up three holes ($60 \times 60 \times 60$ cm^3 in size) and then fill them with their respective soil types. The geophones were deployed 5 m apart so that the rains that hit the different soils can be considered as homogeneous from sensor to a sensor, but at a distance large enough to minimize the interaction between the induced elastic waves and their reflections. For each soil, the geophone was buried at a depth of 10 cm during a first period (27 December 2020–26 January 2021), at 20 cm during a second period (26 January–2 April 2021) and at 30 cm during a third deployment (2

10.1029/2022EA002328

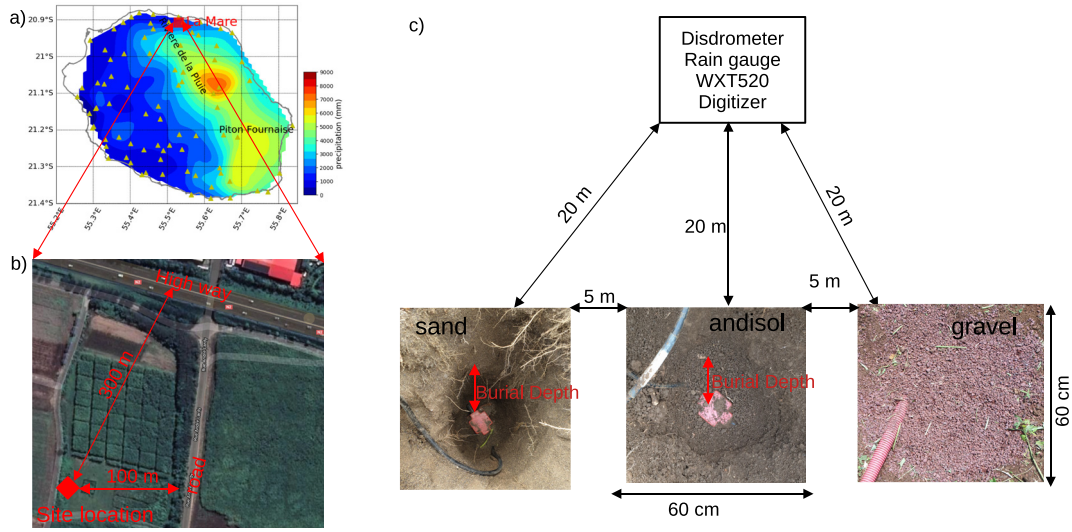

Figure 1. The experimental site. (a) Map of the mean annual rainfall (mm) in La Réunion between 1981 and 2010. The small white triangles show the rain gauges used to measure the precipitation. Those data are from Météo France Réunion. (b) Location of the site on the northern coast of Réunion Island. (c) The different instrumentation used in the present study.

April–5 May 2021). We use a 10 cm difference for each BD to determine at which depth the seismic signal and the rain precipitation best correlate, and for which the effect of the other meteorological parameters (e.g., temperature, humidity) may be considered as not significant. We are aware that the best and easiest setup to investigate the effect of the BD would have been to have installed nine geophones to simultaneously record the same signals at different BD and in different soil types. However, instrumental limitations did not allow us to follow such a procedure. Geophone data were continuously and directly saved with a sampling rate of 1,000 Hz (Nanometrics Centaur digitizer located at a distance ~20 m from each geophone). During the geophone operating time, a rain gauge ARG314 and wind speed measurements WXT520, which also measure other meteorological parameters such as temperature, atmospheric pressure, wind direction, relative humidity, precipitation (Figures S2–S4 in Supporting Information S1), were installed at a distance ~20 m from the geophones. The precipitation rate recorded by the ARG314 sensor with a resolution of 0.1 mm was averaged and saved every minute to a Campbell Scientific CR1000 datalogger. The data from the WXT520 station were also averaged every minute and saved into the same CR1000. We connected a GNSS antenna to the Centaur acquisition for time synchronization.

To characterize the signature of rain on the geophone and particularly its time-frequency response, we computed the power spectral density (PSD) that measures the power of the signal in frequency domain. The time series of the PSD (hereafter we refer as continuous PSD) were obtained by stacking the data together. To calculate the continuous PSD, we used the same routine as proposed by the ObsPy package (Beyreuther et al., 2010). We first divided the time series into 4-min segments overlapping by 50%. Then, each segment was transformed into the time-frequency domain using the method described by McNamara and Buland (2004). The obtained PSD was finally converted into decibels with respect to acceleration (i.e., with respect to $m^2/s^4/Hz$) by removing the geophone response using the poles and zeros provided by Clain (2019, Figure S1).

To estimate the relationship between the seismic data recorded by the geophone and the precipitation rate, we first calculated over a 4 min-long moving window the root mean square (RMS) for each data set, with 50% overlap (more details about the data selections are presented in Section 7). For the seismic noise data, we computed the RMS of the data filtered between 80 and 140 Hz (more details about the lower frequency limit are presented in Section 4.3) and then divided them by the sensitivity of the instruments. We then correlated the two parameters using simple linear regression and computed the transfer function between them.

During the winter season (June–October, 2021), an OTT-Parsivel2 optical disdrometer (Löffler-Mang & Joss, 2000) was installed on the experimental site to observe the rain drop size distribution (DSD) from which other variables can be derived, for example, drop concentration, precipitation rate, radar reflectivity factor, and kinetic energy. The recorded data contains the number of drops, their sizes and velocity measured through a laser

beam of 54 cm^2 in 32 classes of diameters and 32 classes of velocities. The data recorded by the disdrometer was saved every minute to the CR1000 datalogger. In the presence of rain, the volume-weighted mean drop diameter (Dm) (Uijlenhoet & Stricker, 1999) was computed by integrating the data during 4-min.

3. General Overview of the Meteorological Condition of La Réunion

Climate in La Réunion depends on the location of the Intertropical Convergence Zone (ITCZ). La Réunion is warm and humid during the summer season (December–March), with large amount of total precipitation (mean annual precipitation between 1981 and 2010 presented in Figure 1a) associated mostly with storms or cyclones that develop and pass in the neighborhood of the island. The maximum rain is observed on the highest topographies of the island (e.g., Quetelard et al., 2009, and Figure 1a data from Météo France). The April–May season is an intermediate season, which is characterized by more trade winds, bringing moisture to the eastern side of the island (Réchou et al., 2014). During winter (June–August), the southern part of the island is affected by the passage of southern fronts (with an average precipitation of 7 mm/day), while it is dry in the northern with precipitation <1 mm/day (Réchou et al., 2019). In Jun-Aug, the Mascareigne anticyclone generally reinforces, which results in a high frequency of strong trade winds. During spring (September–November), even though the ITCZ is moving southward, La Réunion has a dry season, especially in the West-North-West region.

Figures S2–S4 in Supporting Information S1 show the temperature, atmospheric pressure wind direction, wind intensity, relative humidity, and precipitation from January to May 2021. These figures indicate that for the different seasons the different meteorological parameters change slightly at our location site. These data also show that the year 2021 was rain-deficient and warmer than usual. During the period of geophone deployment at 10 cm BD (Figure S2 in Supporting Information S1), few rain episodes were recorded, with the maximum precipitation of 1 mm/min observed on January 27. During these periods, an intensification of the East-South-East trade winds (direction ∼110°) was observed from 15–19 January, and from 29 January onward, with a peak as high as 9 m/s.

During the period of geophone BD at 20 cm, heavy rains with precipitations as high as 3 mm/min were recorded on 6 and 7 March, which correspond to the passage of the tropical storm Iman close to the island (distance <500 km). These two days were signed with relatively low pressure and intensification of South-South-East wind (direction ∼180°). A period of trade winds was observed from 22 February to 5 March and from 8 to 22 March. An augmentation of temperature was observed during the last few days of March.

Between 1 April to 30 May 2021, the geophones were deployed at 30 cm BD (Figure S4 in Supporting Information S1). In April, there was rain for several days, with trade winds with peak intensity between 4 and 8 m/s, observed most days. In contrast, in May, it was dry in our experimental site with no rain. A relatively weak wind was recorded until 12 May. The intensification of trade winds was observed from 13 May onward, with the maximum intensity (peak >8 m/s) recorded on 20–21 May and a direction from the South-South-East.

The recorded meteorological parameters during Austral winter (June–August, 2021) and spring (September–October, 2021) are presented in Figure S5 in Supporting Information S1. As expected, due to the remoteness of the ITCZ, the Mascarenes Anticyclone was well developed and trade winds were frequent and intense (Figure S5b in Supporting Information S1). It was drizzling from time to time in June–July with precipitation <0.4 mm/min, while in August the weather was dry and no rain was recorded except on 28–29 (Figure S5c in Supporting Information S1). The spring season (September–October) was still characterized by the presence of Mascarene anticyclone and frequent trade winds during this year (Figure S5e in Supporting Information S1). A light rain was also recorded occasionally until October 13 (Figure S5f in Supporting Information S1).

4. Results: Seismic Spectral Analyses

An example of the temporal evolution of the seismic noise recorded by the geophone buried at a depth of 10 cm for the gravel is presented in Figure 2. The continuous PSD recorded by the geophones during January-May are presented in Figure S2–S4 in Supporting Information S1, for the BD of 10 cm, 20 and 30 cm, respectively. In these figures, the 4-min RMS of the wind speed (m/s) and the precipitation rate (mm/min) are plotted in pink and magenta dots, respectively. Figure 2 and Figures S6–S8 in Supporting Information S1 show the intensification of the spectral energy in the presence of rain and wind, at a frequency between 5 and 500 Hz. However, human activities are only observed at frequencies <100 Hz. These figures also indicate that if multiple activities

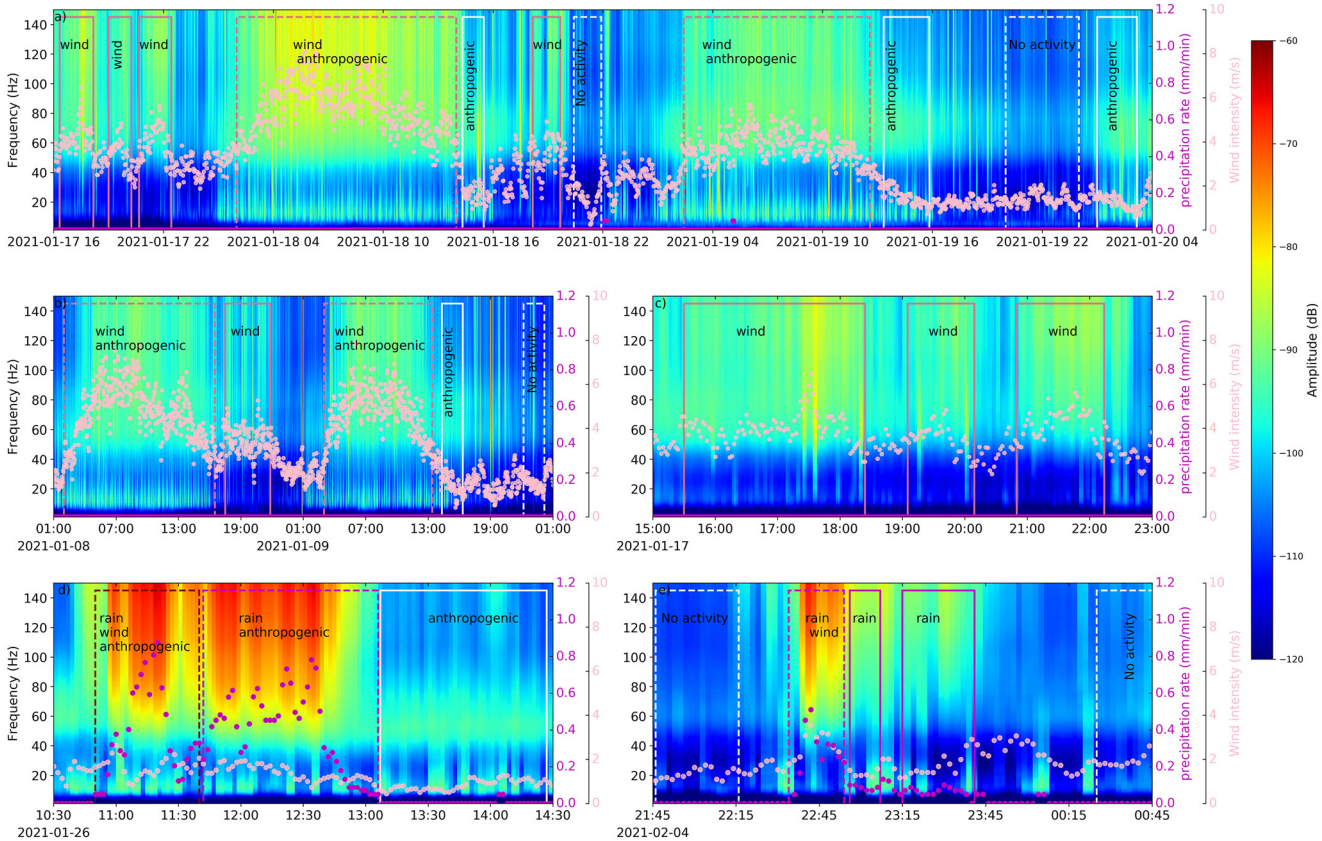

Figure 2. Examples of the time series plot of the continuous power spectral density (PSD) gravel at burial depth of 10 cm. The PSD is defined with respect to acceleration (m^2/s^4/Hz). Magenta dots indicate the 4-min root mean square (RMS) of the rain intensity (mm/min), and pink dots denote the 4-min RMS of the wind intensity (m/s). Each panel underlines the seismic signature of the anthropogenic, wind and rain only or their cumulative response by different boxes. Continuous boxes indicate the periods of single dominant wind (in pink, nighttime period with wind speed >3 m/s and no rain), rain (in magenta, nighttime period with wind speed <2 m/s and presence of rain for a duration >10 min) and anthropogenic (in white, period during the daytime with wind speed <2 m/s and no precipitation) activities. The dashed colored boxes indicate the periods where two (or more) activities overlap: pink (wind + anthropogenic), magenta (rain + anthropogenic or rain + wind) and maroon (rain + wind + anthropogenic). The "no activity" quiet period (inside dashed white boxes) indicates a period during the nighttime (between 20 p.m. and 5 a.m., in local time) with no rain and wind intensity <2 m/s. To avoid over-crowded figures (which mask the PSD response), we did not plot the different rectangles on Figures S2–S4 in Supporting Information S1. Note that the times shown on these plots (and all the following plots) are in GMT and that La Réunion is at GMT+4.

simultaneously occur, their frequency signatures may overlap, and the observed spectra represent their cumulative effects. In the following, we discuss in detail the spectral characteristic of each activity.

4.1. Anthropogenic Seismic Signature

As soon as a seismic station is installed in a region where humans exist, it will record the so-called anthropogenic (or cultural) noise, induced by all the human activities that generate ground vibrations. It covers the signature of traffic, construction, motors, cultural activity, etc. In general, the anthropogenic noise is characterized by stronger energy during daytime and working days than during nighttime and weekends. Anthropogenic noise is typically observed at a frequency range between 1 and 45 Hz (e.g., Díaz et al., 2017; Riahi & Gerstoft, 2015). Analyzing in detail the anthropogenic activities (hereafter called ANT) from the seismic signal is out of the scope of the current study. However, a brief description and discussion of the anthropogenic noise recorded by the geophones are necessary to better decipher the other natural signals we wish to tackle.

Figure 2 and Figures S2–S4 in Supporting Information S1 show that in our experimental site, the anthropogenic noise is stronger between ~5 and 20hr (LT). To characterize the ANT, we first looked for periods (>60 min) with a weak wind (<2 m/s) and no rain activity. Examples of these periods are presented in Figure 2. Our results show that below 2 m/s, the wind activities might still have a minor effect on the recorded seismic spectra (<0.5 dB). However, at the experimental site, the presence of wind activity <1 m/s only occurs during short

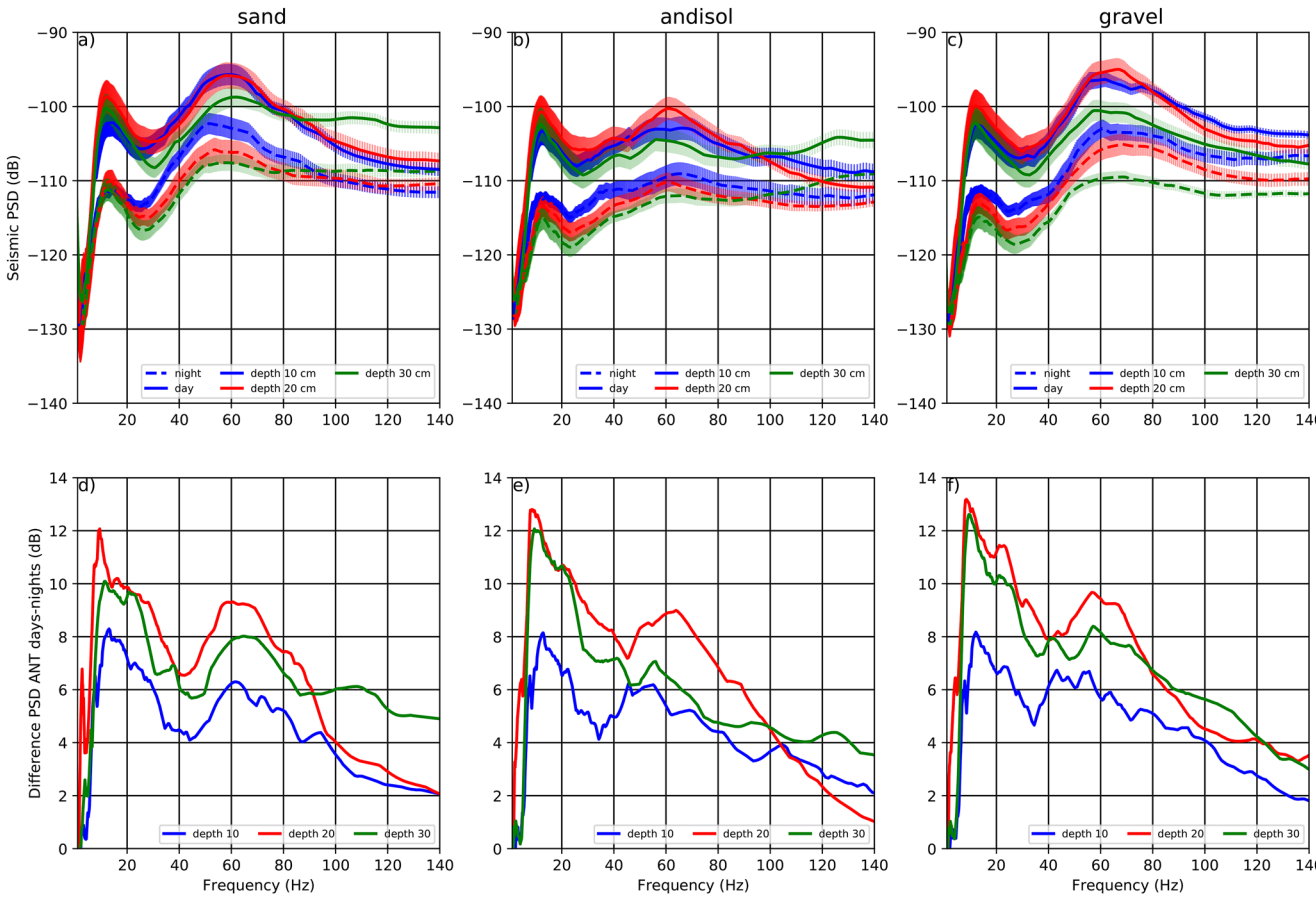

Figure 3. Top: Average power spectrum of anthropogenic seismic noise (ANT) for daytime (continuous line) and nighttime (dashed line) at a burial depth of 10 cm (blue), 20 cm (red) and 30 cm (green), for the (a) sand, (b) andisol and (c) gravel. The vertical lines represent the standard deviation, which we assumed as the errors in the spectrum. Bottom: Difference between ANT activities during the day and night for the three burial depth.

periods (<30 min) during daytime. For each time segment, we computed the average PSD and plotted them in Figure S6 in Supporting Information S1. The medians of the ANT during the daytime and nighttime are plotted in Figure 3, for the different soil types and BD. To evaluate the error in the spectra, we computed the standard deviation of the noise amplitude, for each time segments and for each frequency, and plotted them in Figure 3.

The temporal evolution of the seismic noise presented in Figure 2 suggests that the ANT around the site is recorded at frequencies ~2–100 Hz, and characterized by two dominant peaks observed between ~4–25 Hz and ~40–80 Hz. The former peak is most likely dominated by human activities, while the latter may be affected by the thermoelastic and meteorological conditions (see De Angelis & Bodin, 2012; Tsai, 2011). Human activities at a frequency between ~4 and 25 Hz have been observed in other studies using data recorded by seismometers, with a sampling rate of 100 Hz (e.g., Díaz et al., 2017; Groos & Ritter, 2009). The seismic signature of the anthropogenic activity was observed during daytime between 7 and 15 Hz along a river (the Rivière du Mât) in La Réunion (Gonzalez, 2019). Using a sensor sensitive to higher frequencies, the ANT was recorded at a frequency up to ~100 Hz (e.g., Riahi & Gerstoft, 2015).

Our interpretation of the attenuation of the ANT according to the BD is limited because of the uneven activities for the different periods. Nevertheless, Figures 3a–3c indicate that for each soil type, during the day, the BD 10 cm have a lower (or comparable) energy than the BD 20 cm. These observations are most likely related to the variation of human activities and the meteorological conditions. During school vacations in La Réunion, between 28 December and 26 January, we observed a significant (~5 dB) reduction of seismic noise (not shown here), suggesting that the particularly low energy for the BD at 10 cm is related to holidays.

The difference between the median of the PSD during the daytime and nighttime (5–13 dB) shows similar results, that is, presence of two peaks (Figures 3d–3f), which can be attributed to ANT (<30 Hz) plus the noise due to the variation of the meteorological condition during the day and night for the frequency between 40 and 80 Hz. In addition to the school holiday, we interpret the lowest energy during the BD of 10 cm to the variation of human activities, particularly due to the different governmental restrictions during the Covid-19 pandemic. As an example, a curfew between 18 and 5 hr was imposed starting on 5 March, which strongly limited the traffic at night and reduced the ANT during the nighttime. The reduction of the seismic noise at frequencies <30 Hz during the COVID19 lockdown has been observed in the previous works (e.g., Lecocq et al., 2020; Poli et al., 2020). Overall, our results show that the seismic noise can be used as a proxy of human activities.

4.2. Wind Seismic Signature

To quantify the wind seismic signature (hereafter noted WSS), we analyzed periods with no precipitations. Some examples at the BD of 10 cm for the gravel are shown in Figure 2. In this study, to evaluate the WSS, we used the PSD corresponding to wind speed ≥3 m/s that occurred continuously for at least 1 hr, which is indicated by the continuous (during the night) and dashed (during the day) pink boxes. The choice of this wind speed threshold is motivated by the fact that at a lower frequency (<20 Hz), the WSS is observed on the spectrogram only at velocity >3 m/s (Figure 2 and Figures S2–S4 in Supporting Information S1). This is consistent with the findings from Withers et al. (1996) who found that the minimum wind speed at which the seismic noise appeared to be influenced is 3 m/s for a seismic sensor at the Earth's surface. Alternatively, it is possible that the anthropogenic dominates the signal as suggested by Dybing et al. (2019).

As presented in Section 3, the experimental site is subject to a strong wind during daytime but weaker at nighttime. Figure 2 suggests that during the daytime, the WSS and ANT overlap. Therefore, to interpret the continuous PSD of the WSS, we focus on night data (examples shown in Figure 2c). Figure 2c indicates that a geophone starts to record the wind activity for a speed as low as ∼2 m/s, at least for the frequencies >40 Hz. For the wind speed ≥3 m/s, the WSS is observed for a frequency as low as 10 Hz. The PSD results suggest that the intensification of the seismic energy is linked to the wind intensity. Figures S2–S4 in Supporting Information S1 show that the wind activity is observed up to 500 Hz, with dominant frequency between ∼40 and 360 Hz. However, as mentioned in Section 2, the geophones are characterized by a spurious frequency of 140 Hz, so we will only discuss the results below this frequency.

The continuous PSD recorded by the geophones during their BD of 10 cm in the gravel, with the wind intensity and rain precipitation, are presented in Figure 4a. The average PSD for each windy segment is plotted in Figure S7c in Supporting Information S1 (for gravel at BD of 10 cm), and their medians are presented in Figure 4b. The average PSD for each time segment for the other soil types and different BD are shown in Figure S7 in Supporting Information S1.

Two dominant frequency bands carrying the wind energy are observed at ∼5–30 and ∼40–140 Hz (Figure 4b and Figure S7 in Supporting Information S1). However, for the former frequency range, the medians of the PSD in Figure S7 in Supporting Information S1 indicates that the ANT can be stronger (or comparable) than the wind activity for frequencies <15 Hz. The wind-induced seismic noise energy increases above 40 Hz and remains almost constant from 60 to 140 Hz, indicating that the wind generates the maximum seismic energy visible on the PSD above 60 Hz. Note that wind activity was also observed at frequency <1 Hz, which is consistent with previous works (e.g., Lepore et al., 2016). However, in the current work, we only present the spectra at frequencies >1 Hz, in which the strongest energy was observed.

The difference of the spectra between the medians of the wind and the ANTs activities are presented in Figure 4c. We subtract the ANT activity using their respective median, that is, wind activity during the day—ANT and wind activity during the night—"no activity." The Wilcoxon–Mann U test (Gibbons & Chakraborti, 2020), which is a non-parametric method that tests the null hypothesis, indicates that the spectral difference is statistically significant at a 5% level at frequencies >4 Hz. Figure 4c suggests that the seismic energy of the wind increases from ∼2.5 dB (at 35 Hz) to ∼13 dB (140 Hz). The observed difference between daytime and nighttime, at a frequency between ∼35 and ∼80 Hz, with the nighttime being strong, is most likely due to the difference between the thermoelastic and meteorological conditions during the day and night. At frequency >100 Hz, the seismic energy during the day is slightly stronger than at night, which we attribute to the difference in wind intensity during day

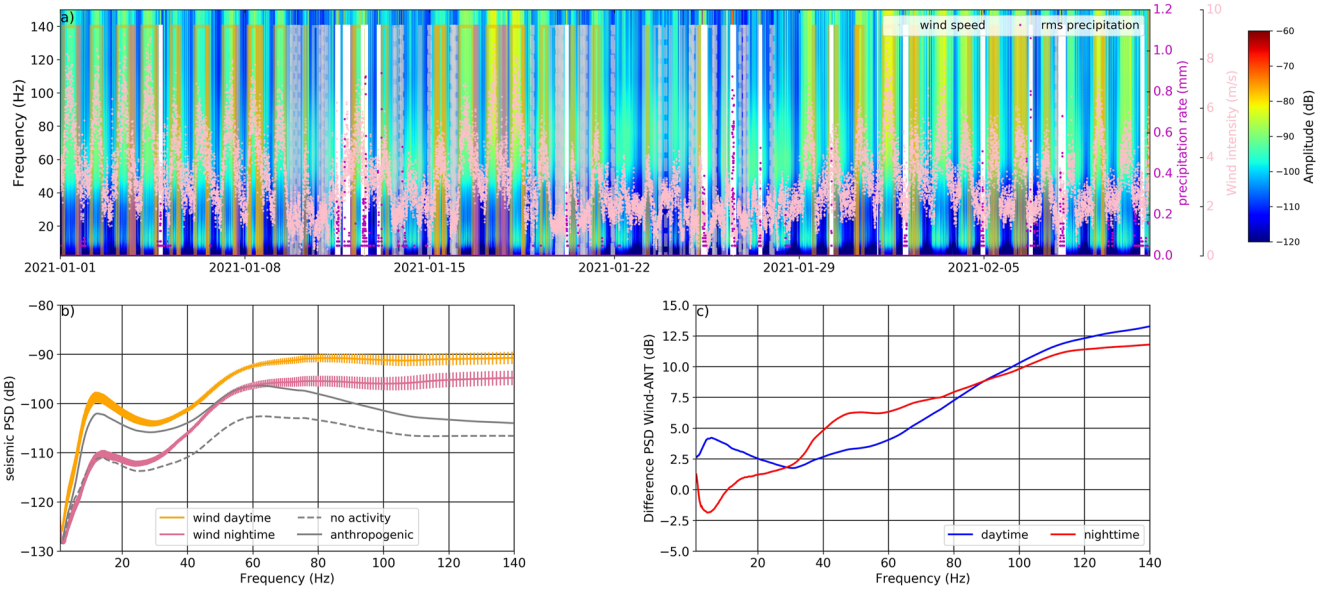

Figure 4. (a) Spectrogram of the seismic data between 1 January and 8 February 2021 for gravel at buried depth of 10 cm. The different rectangles indicate the wind daytime (orange), nighttime (pink), anthropogenic activities (continuous gray) and "no activity" (dashed gray) used to compute the average power spectral density (PSD) in Figure S6 in Supporting Information S1 (anthropogenic) and Figure S7 in Supporting Information S1 (wind activity). (b) Median of the average PSD presented in Figure S7c in Supporting Information S1, together with their standard deviations, for wind activity during the day (orange) and night (pink). Continuous gray line indicates the median of the anthropogenic noise, and dashed line corresponds to the median of the "no activity" quiet periods. (c) Difference between the PSD of the wind activity and anthropogenic noise during the night (red) and day (blue).

and night. In fact, Figure S7 in Supporting Information S1 show that the average wind intensities observed during the night for each time segment are between 3.9 and 4.4 m/s, while during the day, most of the segments have an average wind intensity >4.4 m/s.

The geophones are installed in a site where grasses grow fast; therefore, the observed PSD of the wind is probably a cumulative effect of the direct action of the wind onto the grass and of pressure fluctuations induced by the wind directly on the ground. Although we managed to cut the grass around the site every 2–3 weeks, grass may have affected the data quality and biased some results. Other parameters that could influence the obtained PSD are temperature, atmospheric pressure and humidity. At a frequency of 2.85 Hz, the temperature is known to play a role in the observed seismic noise level (Hillers & Ben-Zion, 2011).

4.3. Rain Spectral Characteristics

Our continuous PSD results (Figure 2d and 2e; Figures S2–S4 in Supporting Information S1) show that the rain activity can overlap in the time-frequency domain with the wind and/or ANT. To investigate the spectral characteristics of the rain, we then considered the data recorded during periods of low wind speed <2 m/s (examples shown in Figures 2d and 2e). These two figures indicate the intensification of the PSD in the presence of rain precipitation >0.025 mm/min. The rain activity is recorded at a frequency range of ~20–500 Hz (Figures S2 to S4 in Supporting Information S1). However, most of the energy is observed between 60 and 480 Hz, in agreement with previous works (e.g., Dean, 2017; Roth et al., 2016). As mentioned in Section 2, the geophones we used are characterized by a typical spurious frequency ≥140 Hz, therefore we will only discuss the results below this frequency.

In the frequency range between 40 and 140 Hz, our results indicate that the seismic energy of the rain increases with the frequency (Figure 5a and Figure S8 in Supporting Information S1). They also show that at frequencies >40 Hz, the observed PSD is well correlated to the precipitation rate (Figures 2d, 2e, and 5a). An exception is observed for the rain episode of January 27 (Figure 5a, blue curve, third row), at frequencies >70 Hz, where one observes the lowest energy (for the daytime), but with precipitation higher than those on January 25. We assume that this difference is due to the difference in humidity on the soil and/or changes in temperature.

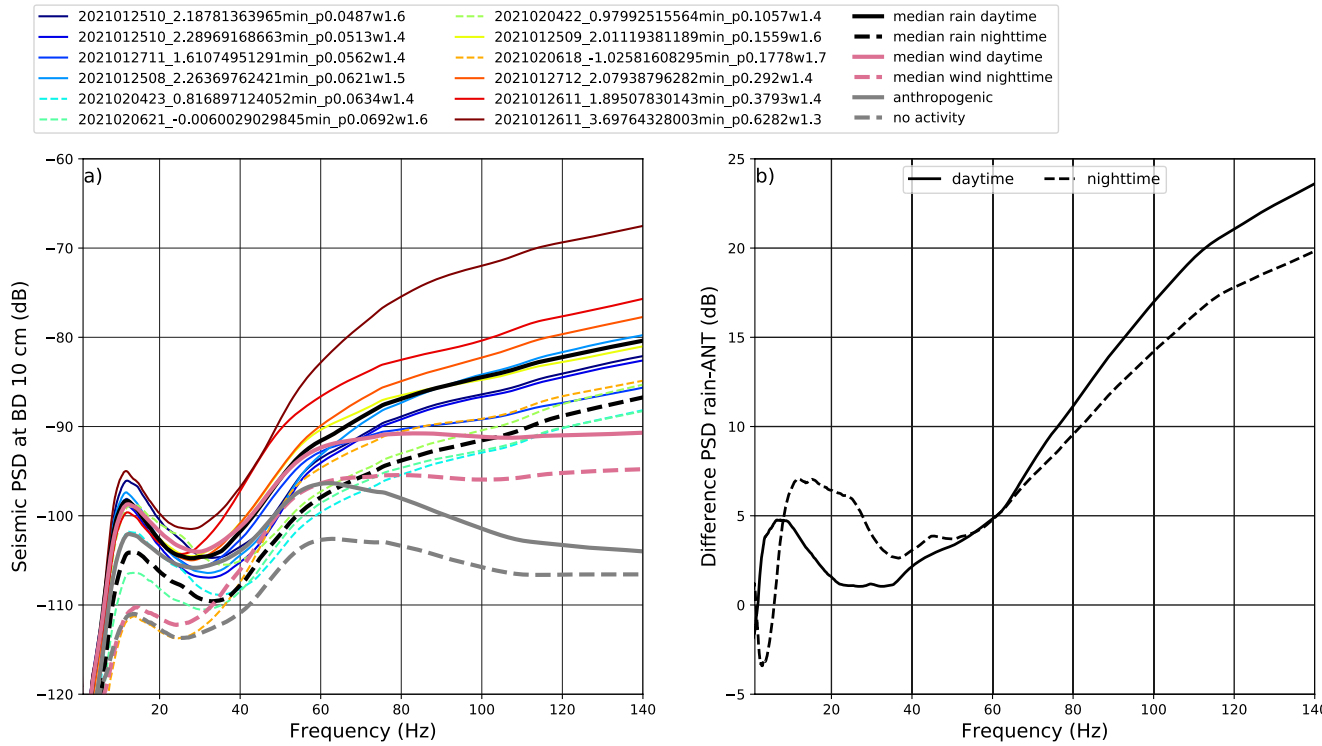

Figure 5. (a) Average seismic power spectral density (PSD) during rain episodes computed at burial depth (BD) 10 cm for gravel. The average PSD for the other BD and soils types are presented in Figure S8 in Supporting Information S1. The average PSDs plotted here, as colored lines, correspond to the rain activities, for periods of low wind intensity (<2 m/s), with rain duration >10 min, during daytime (continuous lines) and nighttime (dashed lines). Spectra are sorted with respect to their intensity, duration and wind speed. For each colored curve, each label shows the starting date of the rain (yyyymmddhh), its duration (in min), average precipitation (mm/min) and average wind intensity (m/s). Black lines indicate the median of the rain during the day (continuous) and night (dashed). Gray lines show the median of the anthropogenic (ANT) noise. (b) Difference between the median of the rain and ANT activities during the day (continuous) and night (dashed).

At frequencies <70 Hz, the median PSD of the rain can be weaker than those of wind during the day and night (Figure S8 in Supporting Information S1), which results in the averaged PSD of the rain (in black) being smaller than those of the wind (in pink) in Figure 5a. We assume that the wind activity dominated the signal until a frequency of ∼70 Hz and that the rain signature becomes dominant above.

As discussed in Section 4.1, the ANT is significant up to 80 Hz, implying that the only parameter that controls the observed rain PSD should be the precipitation. However, Figure 5a shows that at frequencies >80 Hz, having relatively low rain precipitation (compared to those at night), the seismic signature of the rain during the daytime is stronger than those at nighttime (e.g., on January 25, yellow curves, Figure 5a). We assume that these variations are due to the difference in atmospheric conditions, such as temperature and/or atmospheric pressure, during the day and night.

Note that other parameters that likely control the noise level are the rain-droplet size and velocity (e.g., Dean, 2017; Fox, 2004). Unfortunately, our disdrometer was not available during this first experimental deployment, impeding any further investigation of the influence of these two parameters. We discuss in Section 8 such a signature, through a second exploratory deployment in which a disdrometer was simultaneously co-located in the field with the geophones.

To evaluate the seismic energy of the rain, we computed the relative difference between the medians of the rain and the ANT PSD. The obtained difference for the gravel at BD 10 cm is shown in Figure 5b. The difference between the other soil types and BD are presented in Figures S8j–S8l in Supporting Information S1. The null-hypothesis test (not shown here) shows that at frequencies ≥10 Hz, the spectral difference is always statistically significant at 5% level. Our results suggest that the rain activity results in an increase of PSD 5–24 dB, at a frequency ranging from 60 to 140 Hz. Figure 5b (and Figure S8 in Supporting Information S1) displays a rather

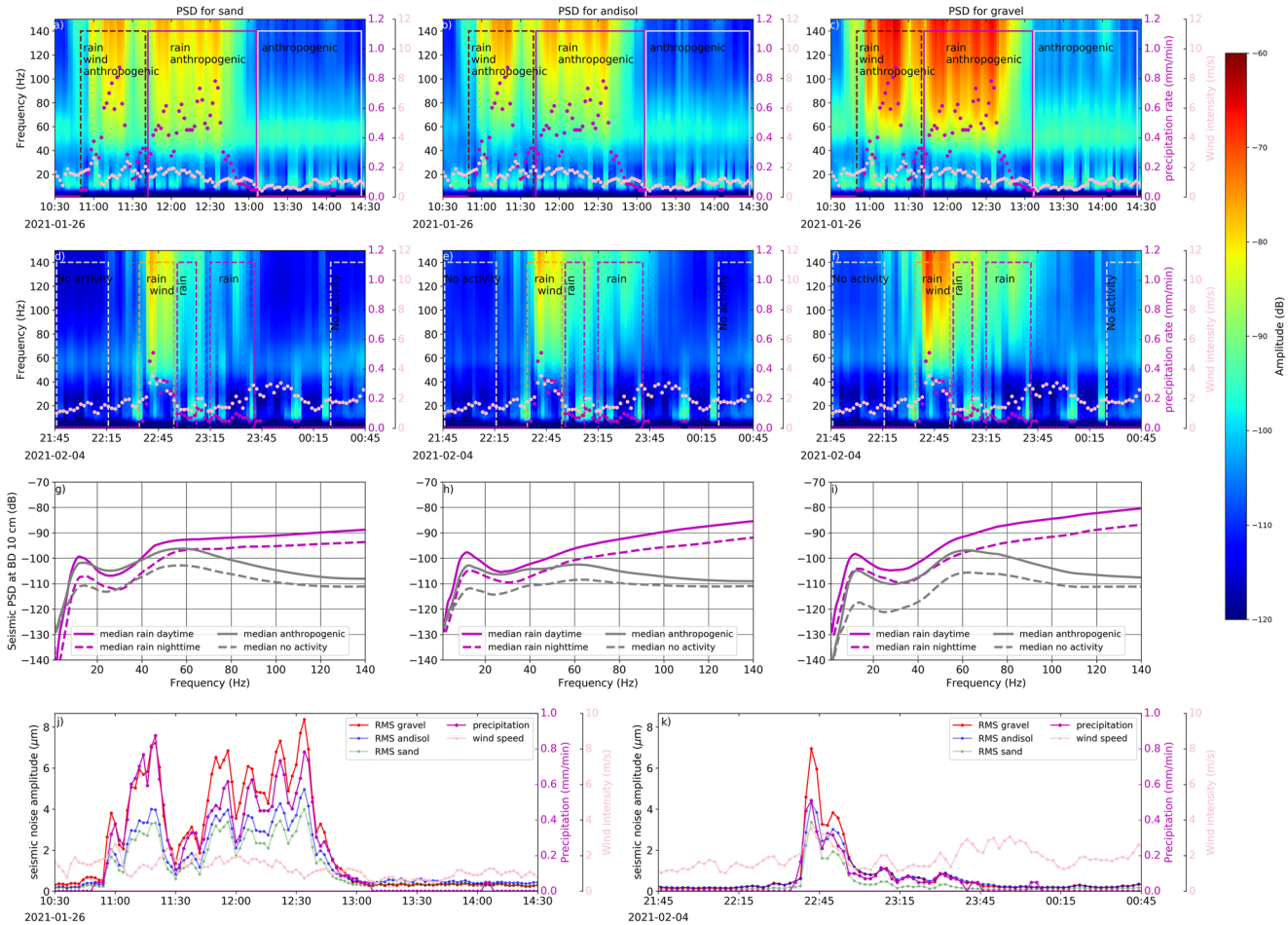

Figure 6. Comparison of seismic noise recorded by geophones buried within different substrates. (a–f) Spectrogram of the seismic data during the daytime on 26 January (a–c) and during the nighttime on 4 February (d–f), for sand (left panel), andisol (middle panel) and gravel (right panel). During these two periods, the geophones were buried at 10 cm. The magenta boxes limit an example of the data used to compute the average power spectral density (PSD) during the daytime (continuous) and nighttime (dashed). (g–i) Median of the average PSD during the rain episodes, for the gravel, at burial depth of 10 cm, during the day (continuous line) and night (dashed line). The gray lines represent the anthropogenic noise. (j–k) Example of the 4-min root mean square of the seismic noise amplitude, at a frequency range between 80 and 140 Hz, for the sand (green), andisol (blue) and gravel (green) together with the rain precipitation (magenta) and wind intensity (pink). Note the clear correlation of the seismic amplitude with the rain precipitation.

low and complex PSD difference between the rain and ANT at a frequency below 60 Hz, but a much clearer linear increase above 60 Hz, which indicates that the rain dominates the noise at increasing frequencies.

The present study shows that the geophone starts recording the rain activity at a precipitation of 0.025 mm/min, in the dominant frequency between 40 and 500 Hz. Below 80 Hz, the rain signature overlap with other activity, while above 360 Hz the seismic signal intensity decreased. We also observed that the strength of the PSD depends on the intensification of the rainfall. The PSD difference between the rain and the anthropogenic noises indicates that the rain signature increases with frequency, with a difference of 24 dB at 140 Hz.

5. Seismic Signature for the Different Soil Types

To investigate the rain seismic signature as a function of the different soil types (nature and rugosity), we analyze the PSD of the rain activity during period of wind intensity <2 m/s and rain duration >10 min. Examples of the obtained PSD and RMS (computed at a frequency between 80 and 140 Hz) for the different soil types at BD of 10 cm are shown in Figure 6 and the 4-min RMS of the seismic amplitude for the different soil types at different BD are shown Figure S9 in Supporting Information S1. Figure 6 shows that the different soils display comparable signatures, with PSD increasing at frequency >40 Hz. However, the intensification of the signal depends on the

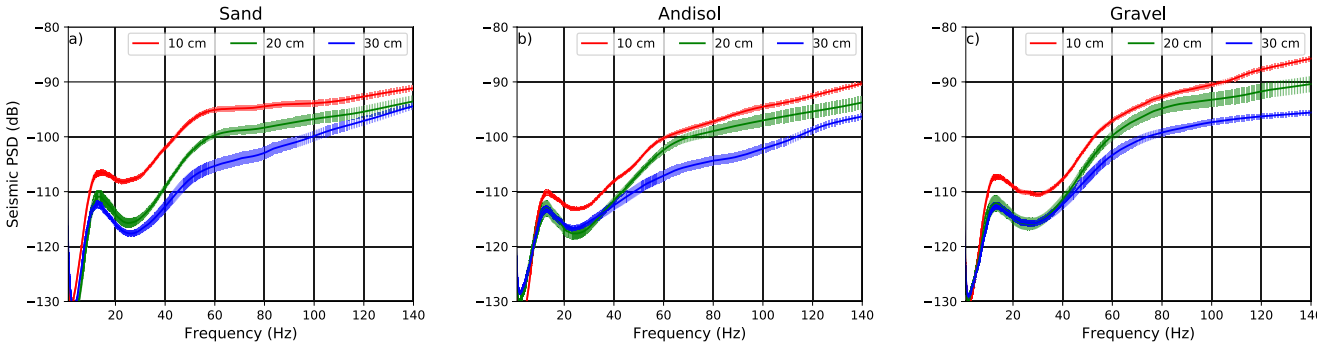

Figure 7. Average seismic power spectral density during rain episodes computed at burial depth of 10 cm (red), of 20 cm (green) and of 30 cm (red), for the different soils, (a) sand, (b) andisol, and (c) gravel. Vertical lines represent the error in the spectrum, which corresponds to the standard deviations. To compute the median, we only included the data with comparable duration, rain intensity and other meteorological parameters. Note that the amplitude of the seismic signal is always lower for larger geophone burying depth.

soil type, characterized by its own signature. Figure 6 (and Figures S8, S9 in Supporting Information S1) shows that at BD of 10 cm, the geophone embedded within gravel displays the strongest signal, then the andisol and the weakest signal is observed for sand set up, suggesting that the strength of the seismic noise is (at least partly) proportional to the granulometry of the soil, at a BD 10 cm and for these three types of soils. However, at the BD 20 cm, Figures S8d–S8f and S9b in Supporting Information S1 indicate that the gravel and the andisol have the strongest and the weakest signals, respectively. The seismic signal of the gravel appears to be the most attenuated at increasing BD, and has the minimum PSD at 30 cm, while the sensor buried in sand displays the highest energy (Figures S8g–S8i and S9c in Supporting Information S1). Our experiments suggest that the soils characterized by large granulometry induce a stronger rain seismic signal at a shallower BD but attenuating with depth. This hypothesis would require further investigation as other parameters that control the observed seismic signal are the local attenuation and/or the intrinsic elastic properties of the medium surrounding the sensor.

6. Sensor Burial Depth and Rain Seismic Signature

As discussed in Section 4, at frequencies >1 Hz, many parameters control the observed PSD, and their signatures may overlap. During the geophones operating time, the meteorological conditions have changed, which likely bias the comparison between the different BD. During the geophone BD at 20 and 30 cm, the wind activities were mostly <3 m/s during the nighttime (see Figure S7 in Supporting Information S1). Therefore, we used the rain data to investigate the variation of the PSD with respect to the BD. To obtain a homogeneous data set for each BD, we selected PSDs that have a comparable meteorological conditions, that is, temperature, pressure and relative humidity. We also focused on data with average precipitation <0.10 mm/min and wind speed <3 m/s. Although the ANT noise mainly affects the data at frequencies <80 Hz, we focused on the nighttime data only in order to reduce its effect. These conditions reduced the effect of the different parameters discussed in Section 4, which could influence the observed noise level for the different BD. The obtained results using these criteria are presented in Figure 7, which shows the median for the PSD, together with their standard deviations, at different BD for sand (Figure 7a), andisol (Figure 7b) and gravel (Figure 7c). Note that in the presence of heavy rain, the site where we installed the geophones was slightly altered by erosion, which removed the upper layer (maximum of 2 cm), indirectly inducing a small change in the actual BD. In addition, the uneven rain characteristics (e.g., kinetic energy, rain drop size) during each BD operating time may also have influenced the obtained results. Furthermore, the slight difference in the rain precipitation for the different BD may have a minor effect on the comparison. To estimate the error in the median spectra, we computed the standard deviation for each time segment. The obtained error ranges from 0.5 to 1.5 dB, at frequencies between 80 and 140 Hz.

The main feature visible from Figure 7 is that increasing the BD decreases the noise level above 20–40 Hz, depending on the soil types. The recorded noise level at a high frequency is systematically of lower amplitude at 30 cm depth than at 20 and 10 cm depth. As discussed in Section 5, each soil has its own signature and its attenuation according to the BD is not the same. For sand, the maximum attenuation of the signal (reduction ~10 dB between the BD 10 and 30 cm) is observed at a frequency between 40 and 80 Hz, which is dominated by the ANT or wind activities (see Section 4). However, for rain response (i.e., frequencies >80 Hz), the signal attenuated

less with respect to the BD with a reduction of PSD <5 dB, between the BD of 10 and 30 cm, at a frequency of 140 Hz. Taking into account the error, Figure 7a indicates that at frequencies >110 Hz, the rain response in the sand for the BD 20 cm and 30 cm can overlap, that is, that signal is weakly attenuated.

Figures 7b and 7c indicate that a difference in BD of 10 cm results in a reduction of the PSD ∼4 and ∼7 dB, at frequencies >80 Hz, for the andisol and the gravel, respectively. The effect of the BD becomes more prominent with increasing frequency for the gravel (and the andisol) with PSD reduction of ∼15 dB (∼8 dB) at 140 Hz, between the BD of 10 and 30 cm. The obtained results agree with the work of Dean (2017) who demonstrated that at frequency between 80 and 250 Hz burying geophones in a clay-rich soil type at 10 cm depth results in an attenuation of the rain noise between 7.7 and 8.6 dB.

Given the fact that human activities were variable during the different BD periods, estimating their reduction with the BD is not possible in the current work. However, Figure 7 suggests that changing the BD from 10 to 20 cm reduced the PSD of the ANT (at frequencies <40 Hz) of ∼5 dB, while changing the BD from 20 to 30 cm have little to no effect on the observed PSD of the ANT. The same results are observed from analyzing the ANT activities in Section 4.1 (Figures 3d–3f). These observations may suggest that burying the geophone at 20 cm is enough to minimize the effect of the anthropogenic noise. Note that evaluating the seismic response of the wind according to the BD was not possible in the present study due to the absence of strong wind activity >3 m/s at night during the geophone BD at 20 and 30 cm (see Figure S7 in Supporting Information S1). However, using a three components geophone, Bland and Gallant (2002) observed comparable attenuation (as the rain obtained here) for the seismic signature of the wind. Their results suggest that burying the geophones at 10 cm reduced the wind seismic signal by ∼4 dB and ∼7 dB in the horizontal and vertical components, respectively.

7. Rain Seismic Signature

The 4-min RMS of the wind speed, precipitation and the seismic noise are plotted together in Figure S9 in Supporting Information S1. Examples of the measured RMS amplitude of the seismic noise recorded by the geophones for the different soil at BD of 10 cm, filtered in the frequency range of 80–140 Hz, together with the precipitation and wind speed, are plotted in Figures 6j and 6k. The scatter plot between the wind speed >3 m/s and their seismic amplitude response are presented in Figures S10 in Supporting Information S1. Figure S9 in Supporting Information S1 indicates that the wind speed <3 m/s and the ANT activities have a minor or no effect on the computed seismic amplitude (<0.07 μm). Their intensities are comparable to the quiet periods of "no activity" during the night. The observed correlation between the precipitation and the seismic noise amplitude, especially in the presence of wind speed <3 m/s (Figures 6j and 6k), suggests that a simple linear regression could be used to quantify their relationship. However, in the occurrence of "strong" wind (speed >3 m/s), the obtained seismic noise includes the wind activity, with a maximum amplitude of 1.4 μm (Figure S10 in Supporting Information S1). Therefore, to compute the transfer function between the precipitation and the seismic ambient noise, we considered data with rain duration ≥10 min and wind speed <3 m/s. The transfer functions between the precipitation and the amplitude of seismic noise, at a frequency range of 80–140 Hz, for the different soil and BD are presented in Figure 8.

Figure 8 indicates that the P_{coef} between the precipitation rate and seismic noise is the lowest (0.84–0.86) at BD of 10 cm, suggesting that other meteorological parameters may still influence the recorded noise at shallow depth, which may bias the correlation between the precipitation and the seismic noise. In contrast, at BD of 30 cm the two parameters correlate much better, with $P_{coef} \geq 0.90$, suggesting a dominant rain signature. Therefore, to isolate the rain response, we suggest that burying the geophone at the depth of 30 cm is sufficient. However, to minimize the rain response (for other seismological purposes, e.g., to determine the transport of sediment in a river), a deeper BD could be necessary as at 30 cm the rain response is still significant, especially if they are buried in a sandy soil.

To validate the transfer functions, we estimated the noise amplitude using the data presented in Figure S11 in Supporting Information S1, for the different BD. In general, the observed and predicted noises are in good agreement within 90%, demonstrating that seismic noise is a good proxy for rain precipitation in this frequency band. An exception is observed in the presence of wind >3 m/s, while the seismic noise amplitude is underestimated, which is due to the wind effect. The difference between the kinetic energy of rain and/or rain drop could also result in the difference between the observed and computed seismic RMS.

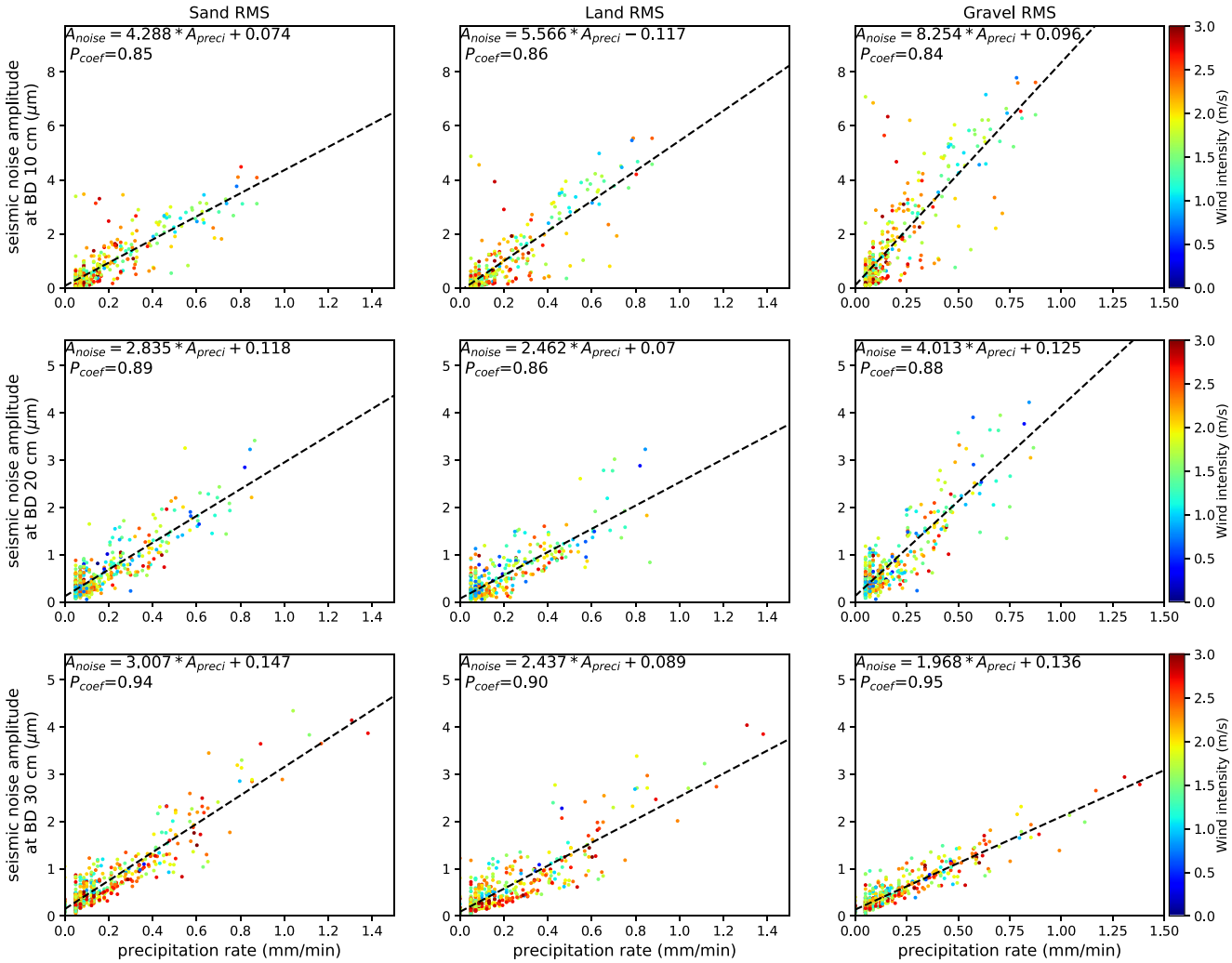

Figure 8. Scatter plot between the root mean square of the precipitation rate and seismic noise amplitude for sand (left column), andisol (middle) and gravel (right column); for the different burial depth 10 cm (top), 20 cm (center), and 30 cm (bottom). The transfer function between the two parameters, which correspond to the dashed black lines are presented at the top left corner, together with the corresponding Pearson coefficient (P_{coef}). The dots colors mark the wind intensity, as indicated on the right scale.

8. Drops Size and Rain Seismic Signature

The continuous PSD for the geophone buried at 30 cm inside the gravel between June and October (i.e., during the winter and spring), together with the different rain parameters characteristics (precipitation rate, volume-weighted mean Dm, kinetic energy) and wind intensity are presented in Figure S12 in Supporting Information S1. The wind intensity is measured by the WXT520 sensor and the precipitation (mm/min) from the rain gauge ARG314. The precipitation rate (mm/h), rain drop size and kinetic energy were calculated using the data measured by a disdrometer. Each parameter was averaged over a 4-min window. Figure 9a shows an example of the PSD between Aug 26 and 31 during rainy episode bringing most of the rain of the month of August.

Figure 9a and Figure S12 in Supporting Information S1 indicate that between June and October, La Réunion is characterized by a strong wind and mild rain (precipitation <0.4 mm/min). During the day, at frequencies >80 Hz, the wind activities dominate the spectra, and there is no remarkable difference between the seismic energy in the presence or absence of rain. Another observation from these two figures is that in the presence of light rain (precipitation <0.1 mm/min, i.e., the rain gauge may not have recorded the tipping every minute, 0.1 being the resolution of the tipping bucket), the seismic signature remains constant despite the presence of rain activity recorded by the disdrometer (e.g., on August 29 at ~23 hr).

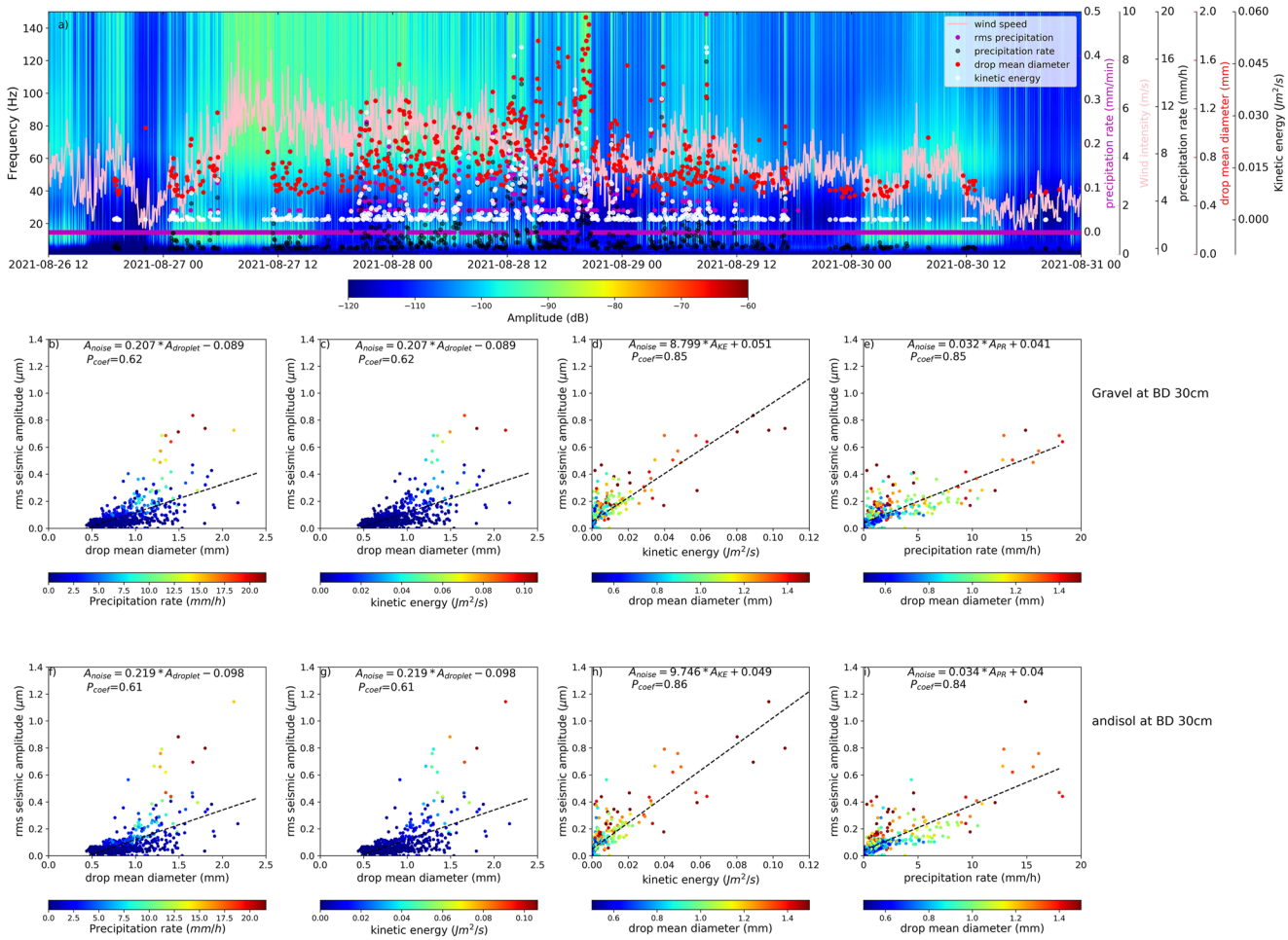

Figure 9. (a): Spectrogram of data recorded by a geophone buried within gravel at 30 cm depth, together with the precipitation rate in mm/min (magenta dots), wind intensity in m/s (pink line), precipitation rate in mm/h (black dots), volume-weighted mean drop size in mm (red dots) and kinetic energy in Jm^2/s (white dots). (b–e) Scatter plot between the root mean square seismic amplitude and the rain characteristic parameters for the geophone buried in the gravel. The seismic data plotted here were acquired during rain episode with low wind intensity (<3 m/s). For each subplot, the color scale of the rain parameters is plotted at the bottom. The equations plotted on the subplots represent the transfer function between the seismic amplitude and the rain characteristic on the horizontal axis, and P_{coef} shows their Pearson correlation coefficient. (f–i) Same as (b–e) but for the andisol.

To investigate the relation between the seismic energy and the different parameters that characterized the rain, we calculated a 4-min RMS (without overlapping) of the seismic noise filtered at a frequency between 80 and 140 Hz and using a 4 min volume-weighted mean Dm. The scatter plots between them are presented in Figures 9b–9e (gravel) and Figures 9f–9i (andisol). Only the data corresponding to wind intensity <3 m/s are shown here. We chose this wind threshold as the presence of wind <2 m/s is limited during the winter. Note that between June and October, there was a technical problem with the geophone buried in the sand. The equations presented at the top of each plot in Figure 9 show the transfer functions between the RMS seismic amplitude and the rain parameters, and P_{coef} indicates the Pearson coefficient between the two parameters.

Figures 9b, 9c, 9f and 9g show that in the presence of precipitation rate <2 mm/hr (or kinetic energy <0.01 Jm^2/s), the amplitude of the seismic noise is <0.07 μm despite the presence of rain drops Dm > 1 mm, which result in a weak correlation between the rain drop size and the seismic amplitude (0.62 for gravel and 0.61 for andisol). However, the RMS seismic amplitude and the kinetic energy (and the precipitation rate) correlate much better, with P_{coef} correlation 0.85–0.86 (with kinetic energy, Figures 9d, 9h) and 0.84–0.85 (with the precipitation rate, Figures 9e and 9i). These observations suggest that in the presence of light rainfall, and at the frequency between 80 and 140 Hz, the main parameters that controlled the recorded seismic energy of the rain are the precipitation rate, then the kinetic energy and finally the drop size for a precipitation rate >2 mm/hr. Note that the observed

seismic signature from light and heavy rainfall has a different energy distribution for a given frequency range (e.g., Ma et al., 2005). Therefore, the obtained results here are only validated for a precipitation <20 mm/hr and within the analyzed frequency ranges.

9. Conclusions

We conducted several experiments to investigate the respective seismic signatures of rain and wind but also of ANT, with different environment setup such as burying depths (BDs) and soil types. The seismic noise recorded by three geophones deployed at different BDs and embedded within different soils types was analyzed, together with different meteorological parameters and with an optical disdrometer, to measure the wind intensity and the rain parameters. Our PSD analysis shows that the ANT dominate the seismic signal at frequency between 10 and 30 Hz, whereas the rain and wind activities are more prominent at frequency >60 Hz with strength >5 dB (at BD of 10 cm).

Experiments with three different soil types (sand, andisol and gravel) indicate that the seismic response of rain is proportional to their granulometry at shallower depth (BD of 10 cm). The rain signal attenuates with increasing BD in the soil with bigger grain size. For BD of 30 cm the sensor in gravel displays the weakest signal.

The results from the different geophones BD indicate that changing them from 20 to 30 cm, have little to no effect on the obtained PSD at frequencies <40 Hz. At shallower depth, other meteorological parameters than wind and rain may influence the recorded seismic noise. The seismic signal at BD of 30 cm correlates well with the precipitation rate and kinetic energy, while the rain-drop size is only proportional to the seismic noise in the presence of precipitation <0.1 mm/min. To efficiently minimize the rain seismic signal (for other seismic studies) the geophone BD should be installed deeper than 30 cm.

From our seismic noise analysis performed in La Réunion, we showed that geophones are an efficient tool to characterize the seismic signature of rain at high frequency. It may be useful in discriminating the difference sources within the various frequency ranges and to better quantify the river activity, particularly the bed load transport during cyclonic floods. The present study will allow further field investigation to improve the estimation of the sediment transport during cyclonic flood events by deploying geophones and seismometers along rivers in La Réunion Island.

Data Availability Statement

The data and softwares used in this study are freely accessible at OSU-R Université de La Réunion, via https://doi.org/10.26171/wpzr-av10 (Rechou et al., 2019; Rindraharisaona, 2021).

Acknowledgments
This study benefited of the support from the Research Federation OMNCG (Observations des Milieux Naturels et des Changements Globaux) and OSU-R (Observatoire des Sciences de l' Univers—Réunion) at the University of La Réunion. This study has been also supported by the ReNovRisk-Erosion FEDER project funded by the Région Réunion and European Community. We thank the CIRAD for the experimental site and the LE2P (Réunion University) for providing the WXT520 sensor. Last but not least, we thank the reviewers, the Editor for constructive comments and suggestions.

References

Bakker, M., Legout, C., Gimbert, F., Nord, G., Boudevillain, B., & Freche, G. (2022). Seismic modelling and observations of rainfall. *Journal of Hydrsology*, *610*, 127812. https://doi.org/10.1016/j.jhydrol.2022.127812

Barthe, C., Bousquet, O., Bielli, S., Tulet, P., Pianezze, J., Claeys, M., et al. (2021). Impact of tropical cyclones on inhabited areas of the SWIO basin at present and future horizons. Part 2: Modeling component of the research Program RENOVRISK-CYCLONE. *Atmosphere*, *12*(6), 689. https://doi.org/10.3390/atmos12060689

Beyreuther, M., Barsch, R., Krischer, L., Megies, T., Behr, Y., & Wassermann, J. (2010). ObsPy: A Python toolbox for seismology. *Seismological Research Letters*, *81*(3), 530–533. https://doi.org/10.1785/gssrl.81.3.530

Bland, H., & Gallant, E. (2002). Avoiding wind noise: How helpful is geophone-burying. In *Proceedings of the CSEG Geophysics* (pp. 1–4).

Bousquet, O., Barruol, G., Cordier, E., Barthe, C., Bielli, S., Calmer, R., et al. (2021). Impact of tropical cyclones on inhabited areas of the SWIO basin at present and future horizons. Part 1: Overview and observing component of the research project RENOVRISK-CYCLONE. *Atmosphere*, *12*(5), 544. https://doi.org/10.3390/atmos12050544

Burtin, A., Bollinger, L., Vergne, J., Cattin, R., & Nábělek, J. (2008). Spectral analysis of seismic noise induced by rivers: A new tool to monitor spatiotemporal changes in stream hydrodynamics. *Journal of Geophysical Research*, *113*(B5), B05301. https://doi.org/10.1029/2007jb005034

Clain, C. (2019). *Etude de la signature sismique de la pluie à La Réunion (Unpublished master's thesis)*. Université de la Réunion.

Dean, T. (2017). The seismic signature of rain. *Geophysics*, *82*(5), P53–P60. https://doi.org/10.1190/geo2016-0421.1

De Angelis, S., & Bodin, P. (2012). Watching the wind: Seismic data contamination at long periods due to atmospheric pressure-field-induced tilting. *Bulletin of the Seismological Society of America*, *102*(3), 1255–1265. https://doi.org/10.1785/0120110186

Díaz, J., Ruiz, M., Sánchez-Pastor, P. S., & Romero, P. (2017). Urban seismology: On the origin of earth vibrations within a city. *Scientific Reports*, *7*(1), 1–11. https://doi.org/10.1038/s41598-017-15499-y

Dybing, S. N., Ringler, A. T., Wilson, D. C., & Anthony, R. E. (2019). Characteristics and spatial variability of wind noise on near-surface broadband seismometers characteristics and spatial variability of wind noise on near-surface broadband seismometers. *Bulletin of the Seismological Society of America*, *109*(3), 1082–1098. https://doi.org/10.1785/0120180227

Faber, K., & Maxwell, P. W. (1997). Geophone spurious frequency: What is it and how does it affect seismic data quality. *Canadian Journal of Exploration Geophysics*, *33*(1), 46–54.
Fox, N. I. (2004). The representation of rainfall drop-size distribution and kinetic energy. *Hydrology and Earth System Sciences*, *8*(5), 1001–1007. https://doi.org/10.5194/hess-8-1001-2004
Gibbons, J. D., & Chakraborti, S. (2020). *Nonparametric statistical inference*. CRC press.
Gonzalez, A. (2019). *Suivi sismologique de l'impact des cyclones sur la charge de fond de la Rivière des Pluies et de la Rivière du Mât à La Réunion* (Unpublished doctoral dissertation, p. 146). Université de la Réunion.
Groos, J., & Ritter, J. (2009). Time domain classification and quantification of seismic noise in an urban environment. *Geophysical Journal International*, *179*(2), 1213–1231. https://doi.org/10.1111/j.1365-246x.2009.04343.x
Guzzetti, F., Peruccacci, S., Rossi, M., & Stark, C. P. (2007). Rainfall thresholds for the initiation of landslides in central and southern Europe. *Meteorology and Atmospheric Physics*, *98*(3), 239–267. https://doi.org/10.1007/s00703-007-0262-7
Helmstetter, A., & Garambois, S. (2010). Seismic monitoring of Séchilienne rockslide (French Alps): Analysis of seismic signals and their correlation with rainfalls. *Journal of Geophysical Research*, *115*(F3), F03016. https://doi.org/10.1029/2009jf001532
Hillers, G., & Ben-Zion, Y. (2011). Seasonal variations of observed noise amplitudes at 2–18 Hz in southern California. *Geophysical Journal International*, *184*(2), 860–868. https://doi.org/10.1111/j.1365-246x.2010.04886.x
Lecocq, T., Hicks, S. P., Van Noten, K., Van Wijk, K., Koelemeijer, P., De Plaen, R. S., et al. (2020). Global quieting of high-frequency seismic noise due to COVID-19 pandemic lockdown measures. *Science*, *369*(6509), 1338–1343. https://doi.org/10.1126/science.abd2438
Lepore, S., Markowicz, K., & Grad, M. (2016). Impact of wind on ambient noise recorded by seismic array in northern Poland. *Geophysical Journal International*, *205*(3), 1406–1413. https://doi.org/10.1093/gji/ggw093
Löffler-Mang, M., & Joss, J. (2000). An optical disdrometer for measuring size and velocity of hydrometeors. *Journal of Atmospheric and Oceanic Technology*, *17*(2), 130–139. https://doi.org/10.1175/1520-0426(2000)017<0130:aodfms>2.0.co;2
Ma, B. B., Nystuen, J. A., & Lien, R.-C. (2005). Prediction of underwater sound levels from rain and wind. *Journal of the Acoustical Society of America*, *117*(6), 3555–3565. https://doi.org/10.1121/1.1910283
McNamara, D. E., & Buland, R. P. (2004). Ambient noise levels in the continental United States. *Bulletin of the Seismological Society of America*, *94*(4), 1517–1527. https://doi.org/10.1785/012003001
Nwe, T. T., & Tokuzo, H. (2010). Sediment transport due to flooding from levee breach: A numerical application of the 2004 Niigata flood. *International Journal of River Basin Management*, *8*(1), 3–14. https://doi.org/10.1080/15715121003714993
Poli, P., Boaga, J., Molinari, I., Cascone, V., & Boschi, L. (2020). The 2020 coronavirus lockdown and seismic monitoring of anthropic activities in Northern Italy. *Scientific Reports*, *10*(1), 1–8. https://doi.org/10.1038/s41598-020-66368-0
Quetelard, H., Bessemoulin, P., Cerveny, R. S., Peterson, T. C., Burton, A., & Boodhoo, Y. (2009). Extreme weather: World-record rainfalls during tropical cyclone gamede. *Bulletin of the American Meteorological Society*, *90*(5), 603–608. https://doi.org/10.1175/2008bams2660.1
Réchou, A., Flores, O., Jumaux, G., Duflot, V., Bousquet, O., Pouppeville, C., & Bonnardot, F. (2019). Spatio-temporal variability of rainfall in a high tropical island: Patterns and large-scale drivers in Réunion Island. *Quarterly Journal of the Royal Meteorological Society*, *145*(720), 893–909. https://doi.org/10.1002/qj.3485
Rechou, A., Fontaine, F. R., Rindraharisaona, E., Stamenoff, P., Rigaud-Louise, F., Boudevillain, B., et al. (2019). SYSMOP: Etude de la signature de la pluie sur les récepteurs sismiques, 2019–2020 [dataset]. OSUR. https://doi.org/10.26171/wpzr-av10
Réchou, A., Narayana Rao, T., Bousquet, O., Plu, M., & Decoupes, R. (2014). Properties of rainfall in a tropical volcanic island deduced from UHF wind profiler measurements. *Atmospheric Measurement Techniques*, *7*(2), 409–418. https://doi.org/10.5194/amt-7-409-2014
Riahi, N., & Gerstoft, P. (2015). The seismic traffic footprint: Tracking trains, aircraft, and cars seismically. *Geophysical Research Letters*, *42*(8), 2674–2681. https://doi.org/10.1002/2015gl063558
Rindraharisaona, E. J. (2021). (February 15, 2021) power spectral density analyse: Geophones data [software]. OSUR. https://doi.org/10.26171/wpzr-av10
Rindraharisaona, E. J., Barruol, G., Cordier, E., Fontaine, F. R., & Gonzalez, A. (2021). Cyclone signatures in the South-West Indian Ocean from two decades of microseismic noise. *Atmosphere*, *12*(4), 488. https://doi.org/10.3390/atmos12040488
Rindraharisaona, E. J., Cordier, E., Barruol, G., Fontaine, F. R., & Singh, M. (2020). Assessing swells in La Réunion Island from terrestrial seismic observations, oceanographic records and offshore wave models. *Geophysical Journal International*, *221*(3), 1883–1895. https://doi.org/10.1093/gji/ggaa117
Roth, D. L., Brodsky, E. E., Finnegan, N. J., Rickenmann, D., Turowski, J. M., & Badoux, A. (2016). Bed load sediment transport inferred from seismic signals near a river. *Journal of Geophysical Research: Earth Surface*, *121*(4), 725–747. https://doi.org/10.1002/2015jf003782
Tsai, V. C. (2011). A model for seasonal changes in GPS positions and seismic wave speeds due to thermoelastic and hydrologic variations. *Journal of Geophysical Research*, *116*(B4), B04404. https://doi.org/10.1029/2010jb008156
Tulet, P., Aunay, B., Barruol, G., Barthe, C., Belon, R., Bielli, S., et al. (2021). ReNovRisk: A multidisciplinary programme to study the cyclonic risks in the south-west Indian ocean. *Natural Hazards*, *107*(2), 1191–1223. https://doi.org/10.1007/s11069-021-04624-w
Uijlenhoet, R., & Stricker, J. (1999). A consistent rainfall parameterization based on the exponential raindrop size distribution. *Journal of Hydrology*, *218*(3–4), 101–127. https://doi.org/10.1016/s0022-1694(99)00032-3
Wilcock, W. S., Webb, S. C., & Bjarnason, I. T. (1999). The effect of local wind on seismic noise near 1 Hz at the MELT site and in Iceland. *Bulletin of the Seismological Society of America*, *89*(6), 1543–1557.
Withers, M. M., Aster, R. C., Young, C. J., & Chael, E. P. (1996). High-frequency analysis of seismic background noise as a function of wind speed and shallow depth. *Bulletin of the Seismological Society of America*, *86*(5), 1507–1515. https://doi.org/10.1785/bssa0860051507